Case Studies in Thermal Engineering 82 (2026) 108098

Contents lists available at ScienceDirect

Case Studies in Thermal Engineering

journal homepage: www.elsevier.com/locate/csite

Influence of contact resistance on thermal behavior of pouch-cell battery modules under partial direct liquid cooling: A numerical study

P.F. Arroiabe [a], J. Berasategi [a,*], M. Larrañaga-Ezeiza [b], G. Vertiz [b], I. Galarza [b], M. Martinez-Agirre [a]

[a] Mechanical and Industrial Production Department, Faculty of Engineering, Mondragon Unibertsitatea, Loramendi 4, E-20500, Arrasate-Mondragón, Spain
[b] CIDETEC, Basque Research and Technology Alliance (BRTA), Po. Miramón 196, 20014, Donostia-San Sebastián, Spain

HIGHLIGHTS

- Validated 3D multi-scale numerical model for pouch-cell modules with partial DLC.
- All model parameters experimentally measured for high physical fidelity.
- Passive component heating can reach 46 % of total heat at high C-rates.
- Inclusion of ohmic and contact resistance heating improves thermal prediction accuracy.
- 5.Findings support improved thermal design of EV battery modules for reliability.

GRAPHICAL ABSTRACT

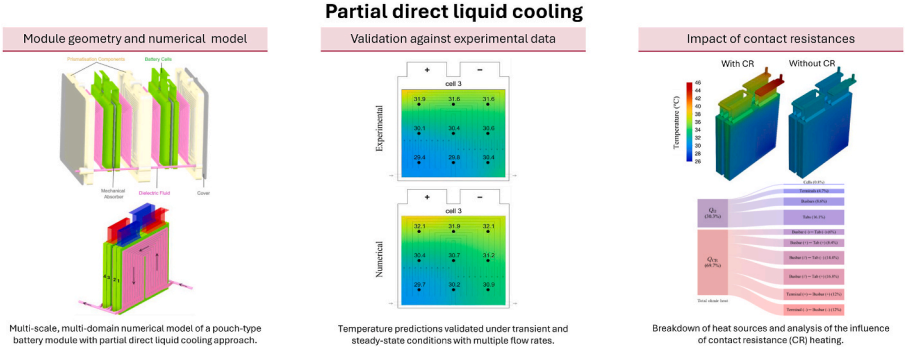

ARTICLE INFO

Keywords:
Direct liquid cooling
Lithium-ion battery thermal management
Pouch-cell module
Contact resistance heating
Numerical case study
CFD
Electric vehicle battery design

ABSTRACT

Direct liquid cooling (DLC) using dielectric fluids is emerging as a highly effective strategy for thermal management in high-performance lithium-ion battery systems, particularly under demanding operating conditions. However, most existing thermal models neglect heat generation from passive components and electrical contact resistances, which can significantly affect prediction accuracy during fast charging and discharging. This work presents a validated 3D multi-scale numerical model of a pouch-cell battery module cooled via a partial immersion DLC approach. The module, composed of four 60 Ah cells in a 2s2p electrical configuration and in a

* Corresponding author.
E-mail address: jberasategui@mondragon.edu (J. Berasategi).

https://doi.org/10.1016/j.csite.2026.108098
Received 25 November 2025; Received in revised form 18 March 2026; Accepted 21 April 2026
Available online 22 April 2026

1s4p hydraulic arrangement, is modeled using a multi-domain framework that integrates electrochemical and thermal phenomena. All model input parameters were experimentally measured in our laboratory, ensuring high physical fidelity. Importantly, the model incorporates ohmic heating in passive components and heat generated by contact resistance, factors often overlooked in existing literature. Validation against experimental measurements demonstrates high accuracy in predicting both transient and steady-state temperature profiles, including spatial temperature distributions within and between cells. Results reveal that passive component heating can momentarily account for up to 46 % of total heat generation under high C-rate charge-discharge cycles, while contact resistance contributes up to 12 % during semi-fast charging. These findings highlight the critical need to include these sources in thermal models to ensure accurate predictions and support design improvements. The proposed approach offers valuable insights for enhancing thermal performance, reliability, and safety of pouch-cell battery modules in electric vehicle applications.

1. Introduction

After the approval of the European Union (EU) ban on the sale of new petrol and diesel cars and vans from 2035, the electrification of the transportation has become a key priority [1]. In addition, the EU is actively legislating to reduce greenhouse emissions by 55 % for 2030 [2], and become climate neutral by 2050 [3]. One of the most fundamental subjects to fulfil these objectives are the Electric Vehicles (EV). A key concern is the increasing demand for energy, power, safety, lifespan, and charging speed in these vehicles, all of which are directly linked to battery performance. To address these requirements, lithium-ion batteries have become the most widely used energy storage technology today.

One of the main obstacles of this kind of batteries is their temperature sensitivity, as performance, degradation, and risk depend on it. Therefore, they should be maintained between 15 and 40 °C [4–6]. Temperatures beyond safe limits may reduce cell capacity, induce internal malfunctions, and escalate into a thermal runaway scenario. Therefore, the thermal management of lithium-ion cells is primordial.

A wide arrange of cooling technologies can be used for this purpose, such as active cooling, passive cooling, phase-change material-based (PCM) cooling, thermoelectric cooling [7] and hybrid cooling [8]. While indirect liquid cooling (ILC) has traditionally dominated thermal management in EVs, innovative approaches are emerging for preserving optimal battery performance, durability and safety. For example, heat pipe cooling, adaptive cooling, multi loop cooling and direct liquid cooling (DLC) technologies have demonstrated their advantages to preserve the temperature within the ideal range. Remarkably, recent years have seen increasingly rapid advances in the field of DLC cooling strategy, which involve the use of a dielectric fluid in direct contact with the heat generation sources—both active and passive components—enhancing thermal management performance compared to ILC methods. It is worth noting that immersion cooling has been highlighted in various review studies as a particularly promising method among direct liquid cooling (DLC) techniques [7,9].

Several studies have investigated immersion cooling at the cell level, employing both single-phase [10–13] and two-phase dielectric fluids [14–18]. Moreover, research has extended this cooling strategy to the module and pack levels, encompassing both experimental and numerical approaches. The following sections provide a structured review of these contributions, beginning with experimental studies and subsequently addressing numerical investigations, each categorized according to the cell format used.

From the experimental point of view, most of the studies have tested cylindrical battery packs [19–24]. Comparing with ILC, all studies stated better temperature control of cells. For example, comparing to air cooling, Satyanarayana et al. [25] observed reductions up to 51.5 % of the maximum battery pack temperature of 20 cylindrical cells for a 3C rate. Similar reductions were demonstrated in the experiments of Chen et al. [24] and Liu et al. [26] for 4C and 3C, respectively. Furthermore, Liu et al. [21] compared the performance of two different dielectric fluids—mineral oil and natural ester oil—for a 4 cylindrical cells battery module. They showed the applicability of the ester one in the immersion cooling strategy. Recently, González-Agirre et al. [22] examined both numerical and experimentally a battery pack of cylindrical cells using a novel tab cooling strategy. Under 4C-rate charge, they obtained a temperature jump reduction of 67 %.

Regarding pouch cell battery packs, one of their main issues is the temperature non-uniformity among individual cells. As in the cylindrical technology, immersion cooling technology also improves the cooling capacity of these modules [27]. Interestingly, Wang et al. [27], using a transformer oil, experimentally observed a considerably temperature difference reduction of 71.2 % under 2C discharge rates. Importantly, both pouch experimental tests showed superior temperatures in the areas closest to the tabs. Nevertheless, authors did not analyze in depth the origin of these heterogeneities. Furthermore, very little attention is paid to the scalability, power consumption and energy density on these experimental studies. To address this question, the authors of this study previously published an experimental investigation on partial immersion cooling of a fully modular and scalable pouch-type battery pack [28]. Under 1.5C-rate charge and discharge pulses, hot spots on zones closest to the passive elements were observed. Unfortunately, considering just the experimental data, the origin of this phenomenon was only analyzed in an indicative way. Consequently, the numerical research adopted for the present study allows this aspect to be evaluated in detail.

From a numerical perspective, several studies have demonstrated the capability of immersion cooling to meet high thermal demands, using self-validated models across various cell types. As in the experimental case, most of the developments were made for cylindrical battery packs [29–37]. Dubey et al. [37] demonstrated that their DLC approach with Novec 7500 fluid achieved 3 times

higher thermal conductance and 15–25 times lower pressure drop than ILC at 3C rate. Similarly, Wu et al. [35] observed at 2C a temperature drop of 7.2 °C comparing to the 29.7 °C obtained on ILC. However, it is important to highlight the significant discrepancy between the numerical model and the experiment results (6.5 °C), as well as the fact that the heat generation experimental values obtained experimentally were used for validation, [36], rather than the temperature values. Other authors have designed innovative immersion cooling battery packs using new flow circuits [31,33], fins [29] and tubes [32]. It should be noted, however, that temperature non-uniformity is not a major concern in cylindrical cells.

In the case of prismatic battery modules, there are few numerical studies where DLC is applied [38]. Okaeme et al. [39] analyzed a battery pack (2p9s or 2p12s) of a hybrid truck using Reduced Order Models (ROM). The temperature with parallel configuration was retained below 55 °C with a standard deviation of almost 0.6 °C under 3C rates. The validation focused exclusively on heat generation, voltage and average temperature, achieving differences below 1 %. Using the same multi-domain ROM framework, Hussain et al. [40] studied an innovative channeled immersion cooling for titanate oxide prismatic cells pack. Interestingly, the results were very close to the experiments (1.5 % for temperature), and they remarkably maintained the maximum temperature below 50 °C under 5C-rate. Nevertheless, it should bear in mind that the validation was limited to average temperature values, thus neglecting the spatial distribution within individual cells.

Finally, regarding pouch type-based battery packs numerical studies, Li et al. suggested a 3D numerical model for 18 LFP cell battery pack. They claimed that, although ILC strategy is not suitable for 10 C-rates, immersion cooling can preserve the maximum temperature below 35 °C, obtaining an excellent thermal uniformity. Same cells pack was tested by Wang et al. [41], but in this case water was circulated throughout internal tubes to cool down the dielectric fluid. In contrast to the previous case, this strategy was not able to cool the pack effectively [40]. Choi et al. [42] created a model of a hybrid battery module combining immersion cooling, thermal interface materials (TMS) and fins. While maintaining a nearly equal gravimetric energy density with the ILC strategy, a reduction of 6.7 °C in maximum temperature and 3 °C in thermal heterogeneity was observed under a 3C-rate. Moreover, the power consumption decreased by 61 %. Patil et al. [11] examined numerically different cooling methods, including a mixed air and immersion cooling strategy. As in the previous cases, the selected strategy reduces the maximum temperature from 40.4 °C to 36.7 °C when compared to the ILC strategy at 5C-rate.

It is worth mentioning that, to date, the effect of the ohmic heat generated in the passive components (terminal, busbar and tabs) was only considered by Patil et al. [11]. However, the thermal effects arising from contact resistance between passive components were not considered in the numerical models. Nevertheless, Wu et al. [43] indicated that the principal source of thermal heterogeneity within the pouch-type large-format cell itself could arrive from the tab, which could be the result of both the current conduction and the contact resistance. In the same line, Ghalkhani et al. [44] also attributed the hot spot location to the resistance between the current collectors and the terminals. Both studies were limited to a single pouch-type cell numerical model. Therefore, as the aforementioned immersion cooling studies were focused on high C-rate scenarios, a high influence of the ohmic heat generated on the passive components is expected. So far, the effect of this heat source has received scant attention in the research literature, particularly in module-scale analyses (as illustrated in Ref. [45]).

Overall, the findings indicate that DLC provides enhanced thermal management capabilities relative to standard ILC systems employed in EV applications. Nevertheless, the implementation of partial immersion cooling strategies has been minimally investigated in the current body of literature. Furthermore, these studies present some limitations. On the one hand, the impact of the ohmic heat of the passive elements on the temperature non-uniformity observed in experimental tests is understudied, particularly for pouch-type battery packs. On the other hand, numerical modeling efforts have seldom incorporated ohmic heating, and the role of contact resistance (CR) as a heat source is largely overlooked. However, this heat source could be a contributing factor to both high maximum temperature and non-uniformities in battery packs, mainly at high C-rates. Thus, the objective of this study is to analyze the influence of the CR heat on the thermal performance of a fully modular and scalable battery module design for EVs with novel cooling system solution based on partial immersion. To carry out the analysis, a 3D multi-scale and multi-domain ROM numerical model is developed. This model not only considers the electrochemical heat generated in the active region, but also the ohmic heat generation within the passive components and at their electrical contacts. Using the numerical model, the thermal behavior of the battery module is analyzed, including the temperature non-uniformity within individual cells and between cells, thereby providing valuable insight into the different heat sources of the module.

Table 1
Cell general characteristics.

Parameter	Value
Nominal voltage	3.68 V
Minimum voltage	2.7 V
Maximum voltage	4.2 V
Nominal capacity	60 Ah
Charging maximum current	120 A
Discharging maximum current	180 A
Charging temperature range	10—35 °C
Discharging temperature range	20—50 °C
Chemistry	Li-NMC
Dimensions	226 × 227 × 12 mm^3
Mass	1.140 kg

The first section of the paper describes the proposed immersion cooling strategy. In the second section the numerical model is defined. After validating the numerical model using temperature contours at different flow rates, an analysis of the various heat sources is presented in the third section quantifying the influence of the CR heat on the thermal performance of the battery module. Finally, the main conclusions of the study are presented.

2. Battery module description

The battery module is described in detail in our previous study. In this section the main characteristics are described. For more information, please refer to Ref. [28]. A large format 60 Ah NMC pouch-type cell was selected, which can improve the packaging efficiency and increases energy density due to its flexibility. Table 1 shows the general characteristics of the cell.

As it was mentioned in the Introduction section, the battery module is chilled using the DLC immersion cooling strategy. However, with the aim of improving the energy density, unlike the most immersion approaches, only one cell surface is in contact with the fluid instead of the entire surface. This solution is referred to as a partial DLC strategy. In particular, the module consists of 4 battery cells, and it is a scale-up of the cell level prototype presented in our previous paper [13], which preserves the prismatisation concept. Fig. 1 shows the module level prototype assembly (Fig. 1a) and the actual image of the module (Fig. 1b). Three prismatisation components were defined: two are situated on the borders with one flow pattern, while the prismatisation of the center is equipped with channels on both sides. Thus, any number of modules could assembly linearly pragmatizing the intermediate component.

2.1. Testing boundary conditions

Consistent with our previously published experimental investigations at both the cell [13] and module level [28], the fluid inlet and ambient temperatures were set to 25 °C. The applied flow rate range (0.3–1.5 L min^{-1}) was selected to encompass a broad spectrum of operating conditions, using 0.9 L min^{-1} as a reference point, as it provides a balance between thermal performance and pumping power consumption. Furthermore, the thermal analysis was performed under two distinct tests conditions: a steady state 1.5C pulse test and a transient profile which includes a 1.6C semi-fast charging profile that represents an electric bus operation (Fig. 2).

On the one hand, a constant 1.5C-rate profile was applied between 50 % and 60 % SOC (state of charge) to maintain uniform heat source during energy input and output operations. Fig. 2a presents the current and SOC profiles of the module for the steady pulse profile. It is worth noting that there is a minor difference in the heat generation between the different operation periods [13]. Even so, the thermal behavior reaches to a semi-stationary state enabling the thermal performance analysis discarding the electro-thermal dynamic effects.

On the other hand, a reference driving profile for an electric bus is applied, which includes a 1.6C semi-fast charging region. As Fig. 2b shows, the profile integrates a C/4 discharge from 100 % to 20 % SOC, an additional 1.6C semi-fast charge from 20 % to 90 % SOC, a C/4 discharge from 90 % to 20 % SOC and finally a C/4 charge from 20 % to 100 % SOC.

3. Numerical modelling description

Fig. 3 presents a schematic overview of the numerical model architecture. The battery is modeled using a Multi-Scale Multi-Domain (MSMD) approach, incorporating data obtained from cell characterization. In parallel, the CFD model solves the governing equations

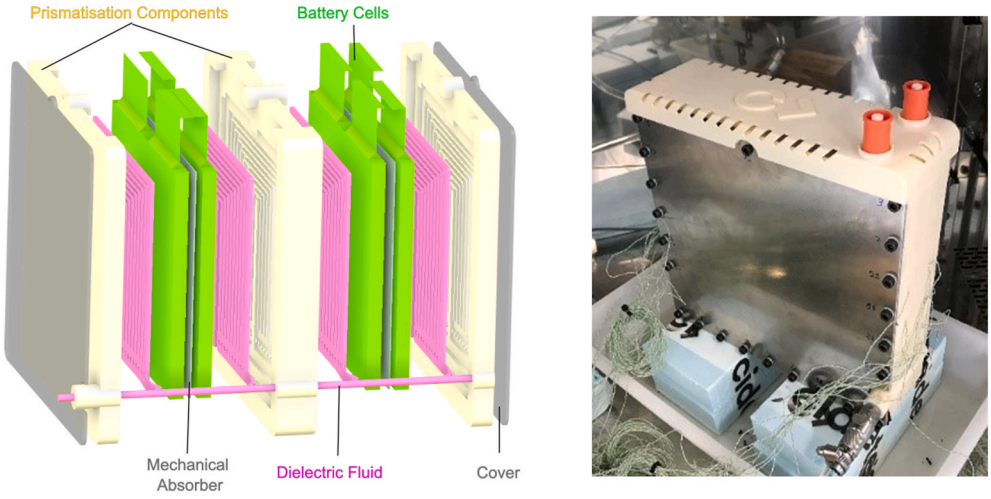

Fig. 1. 2p2s DLC battery system, a) module level assembly, b) real prototype.

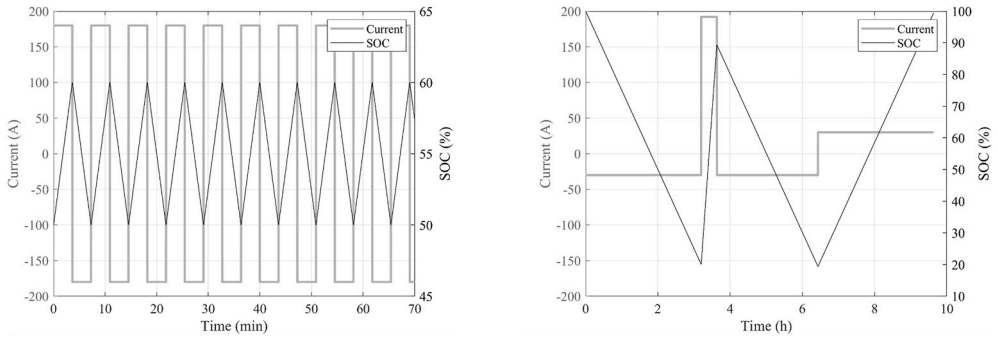

Fig. 2. Current and SOC profiles of the battery module: (a) Steady-state pulse condition, and (b) Transient condition.

for both fluid and solid domains. These two models—battery and CFD—are integrated using a ROM methodology.

3.1. MSMD model

To properly model the behavior of electric batteries, an efficient model which integrates both electrical behavior and thermal generation of the cell in a multi-physics and multi-domain environment is needed. For this purpose, in the present study MSMD approach proposed by Kim et al. [46] is used for coupling the transient behavior of electrical and thermal phenomena of the battery cell. The reliability of this method for modelling the electrothermal behavior at cell level was demonstrated in our previous study [13]. In this framework, the battery module is organized in two different regions: active and passive zones. Active zones consist of the active material, while the passive zones are the positive and negative tabs, connection busbars and terminals. Thus, the energy equation of these zones is as follows:

$$\frac{\partial \rho C_p T}{\partial t} - \nabla \cdot (k \nabla T) = \sigma_+ |\nabla \varphi_+|^2 + \sigma_- |\nabla \varphi_-|^2 + \dot{q}_{\mathrm{ECh}} \qquad \text{Eq. 1}$$

where ρ, k and C_p are the density, thermal conductivity and specific heat of the cell, T is the temperature, and t is the time. The terms on the right-hand side represent the different terms of the heat generation of the battery cells circuit. In particular, the first two terms account the ohmic heating, where σ_+ and σ_- are the electrical conductivities of the positive and negative electrodes, respectively; whereas φ_+ and φ_- are the phase potentials of positive and negative electrodes, respectively. Finally, the last term represents the

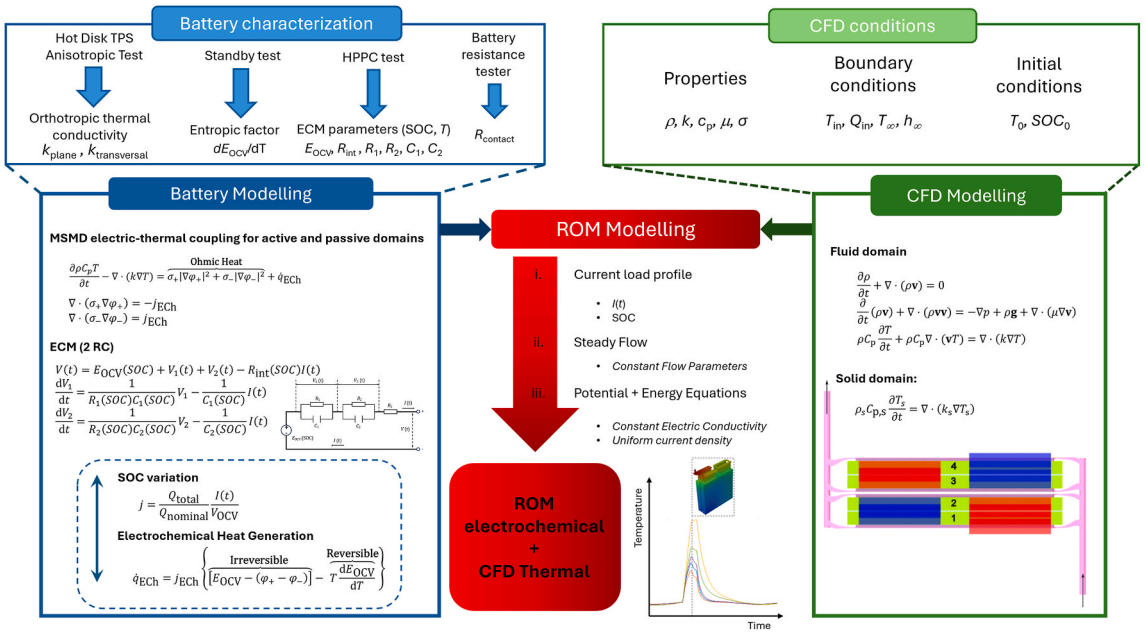

Fig. 3. Schematic description of the Multi-Scale Multi-Domain numerical model.

volumetric heat generation because of the electrochemical reactions ($\dot{q}_{ECh}$).

Due to their layered structure—formed by stacking electrodes and separators—pouch-type cells exhibit anisotropic behavior, with differing thermal conductivities in the transverse and planar directions. Consequently, their thermal conductivity is orthotropic. To determine it, a Hot Disk TPS Anisotropic Measurement Module was used, which complies with the international standard ISO 22007-2 [47]. Table 2 presents the thermophysical properties of the components and the dielectric fluid.

In the MSMD approach, the current density and potential equations are solved in the electrode scale in both active and passive zones. The current density variation is solved using Eq. (2a) and Eq. (2b):

$$\nabla \cdot (\sigma_{+} \nabla \varphi_{+}) = -j_{ECh} \quad \text{Eq. 2a}$$

$$\nabla \cdot (\sigma_{-} \nabla \varphi_{-}) = j_{ECh} \quad \text{Eq. 2b}$$

where j_{ECh} denotes the volumetric current transfer density due to the electrochemical reaction. Both $\dot{q}_{ECh}$ and j_{ECh} are computed using an electrochemical submodel. In the present study the Equivalent Circuit Model (ECM) is employed to compute both terms. This model mimics the electric behavior of the battery by an electric circuit. In this case, the six parameter ECM model suggested by Chen et al. [48] is adopted (Fig. 3). This model comprises three resistive and two capacitive components, effectively capturing the dynamic electrochemical behavior. Thus, the voltage-current connections can be determined using Eq. (3):

$$V(t) = E_{OCV}(SOC) + V_1(t) + V_2(t) - R_{int}(SOC)I(t) \quad \text{Eq. 3}$$

Here, V symbolizes the terminal voltage, E_{OCV} the open circuit voltage, which considers the voltage variation with SOC without any load, $V_1(t)$ and $V_2(t)$ are the voltage across the first and second parallel RC loop, respectively, R_{int}, denotes the ohmic polarization of the cell and $I(t)$ represents the transient current load. Both voltages across the loops can be obtained using the following equations:

$$\frac{dV_1}{dt} = \frac{1}{R_1(SOC)C_1(SOC)}V_1 - \frac{1}{C_1(SOC)}I(t) \quad \text{Eq. 4a}$$

$$\frac{dV_2}{dt} = \frac{1}{R_2(SOC)C_2(SOC)}V_2 - \frac{1}{C_2(SOC)}I(t) \quad \text{Eq. 4b}$$

In Eq. (4a) and Eq. (4b), R_1 and R_2 are the resistances and C_1 and C_2 the capacitances of the first and second RC loops, respectively. In the present study, all the parameters depend on SOC and temperature.

Because of the non-ideal contact between the connection surfaces, contact resistances appear between passive components, which depend on many different parameters such as surface nature and material, and the employed welding technology. As in the present study high current load profiles were employed, the CR heat generated in these surfaces could have a significant impact on the temperature non-uniformity within the cells. Thus far, the influence of contact resistance-induced heat on passive components (terminals, busbars and tabs) has not been comprehensively addressed in either experimental or numerical research. Therefore, the present study explores, for the first time, the effects of the ohmic heat sources on a battery module cooled by the DLC strategy. The contact resistance (CR) values used in this study were experimentally measured using a Hioki BT3554 Battery Tester at 1 kHz AC. It is important to note that CR values can vary depending on several factors such as surface roughness, material properties, welding technique, applied pressure, and operating temperature. Therefore, the values adopted in the model correspond to the specific assembly and testing conditions of our prototype. Moreover, only a limited number of studies have experimentally quantified contact resistance in battery interconnects, and these typically focus on isolated joint types. For example, Brand et al. [49] reported tab-joint CR values of approximately 0.13–0.35 mΩ depending on the welding configuration, whereas Choi et al. [50] documented tab-to-busbar resistances on the order of 0.60–1.20 mΩ for 0.3 mm Al tabs connected to Al/Cu busbars. The contact resistances measured in our prototype lie below these ranges, which is consistent with the high metallurgical quality and cleanliness achieved in our welded interfaces. This agreement further supports the suitability and internal consistency of the CR inputs used in the present model.

The resistance values are summarized in Table 3.

In the ECM model, the variation of SOC for a transient current load can be determined by the following equation:

Table 2
The thermophysical properties of the materials defined in the numerical models.

Property	Cell	Cathode(+Tab)	Anode (-Tab)	Busbar	Dielectric fluid	Module housing	Mechanical absorber
Density (kg/m^3)	1852	2719	8978	8978	774.1	1240	250
Heat Capacity (J/kgK)	1046	871	381	381	2130	1300	1500
Thermal conductivity (W/mK)	Planar: 17.9 Trans.: 0.65	202.4	387.6	387.6	135	0.175	0.07
Electrical conductivity (S/m)	-	3.5e7	5.8e7	5.8e7	-	-	-
Kinematic Viscosity (mm^2/s)	-	-	-	-	4.3	-	-

$$\frac{\mathrm{d}}{\mathrm{d}t}(\mathrm{SOC}) = \frac{I(t)}{3600 Q_{ref}} \quad \text{Eq. 5}$$

where Q_{ref} is the battery reference capacity. For this study, the reference capacity of each cell was 60 Ah (Table 1).

To predict the dynamic performance of the battery and determine the parameters of the ECM model, High Power Pulse Charging (HPPC) tests were carried out. The experiments were conducted at two distinct ambient temperatures (25 °C and 45 °C), applying both charge and discharge pulses to the cell at discrete SOC levels ranging from 0 % to 100 % in 10 % increments. After that, the parameters for the ECM model were obtained using the Least Square method.

Once known the voltage at the cell scale, the coupling between the MSMD and the ECM is carried out using the transient volumetric current density, which is determined as follows:

$$j = \frac{Q_{\mathrm{total}}}{Q_{\mathrm{nominal}}} \frac{I(t)}{E_{\mathrm{OCV}}}. \quad \text{Eq. 6}$$

where Q_{total} and Q_{nominal} refers to the total and nominal capacity of the cell, respectively. In this case, the modeled cell is equal to the experimental one, so both values are identical. Finally, the volumetric heat generation due to the electrochemical reaction is determined. For this purpose, the generated heat is divided into two different terms: irreversible and reversible heat. On the one hand, the irreversible heat considers the heat due to the voltage overpotential (first term on the right-hand side of Eq. (7)), while the reversible heat is determined considering the entropic heating (second term on the right-hand side of Eq. (7)).

$$\dot{q}_{\mathrm{ECh}} = j_{\mathrm{ECh}} \left\{ [E_{\mathrm{OCV}} - (\varphi_{+} - \varphi_{-})] - T \frac{\mathrm{d}E_{\mathrm{OCV}}}{\mathrm{d}T} \right\}. \quad \text{Eq. 7}$$

The entropic factor of the reversible heat generation was experimentally determined analyzing the Open Circuit Voltage (OCV) variation with the temperature ($\mathrm{d}E_{\mathrm{OCV}}/\mathrm{d}T$). This process is named standby process, and it is used to calculate the variation of voltage based on temperature changes at different SOC levels. This methodology is especially suitable for large-capacity pouch cells because maintaining a fixed and uniform temperature minimizes relaxation times and improves measurement stability and accuracy. In this case, the experiments were carried out at 25 °C. Although the entropic coefficient may slightly depend on temperature, the operating thermal window of our study is narrow, and the resulting variation of the reversible heat term is expected to be negligible compared to the total contribution. For this reason, the values obtained at 25 °C are considered sufficiently representative for the thermal conditions investigated in this study. Fig. 4 presents the entropic factor variation for different SOCs.

3.2. CFD model

After determining the heat generation of the cell, the behavior of the dielectric fluid was modeled. The dielectric fluid flows through the inlet of the designed module contacting directly with the active cells. Thus, the equation of continuity (Eq. (8a)), momentum (Eq. (8b) considering laminar flow) and energy (Eq. (8c)) are as follows:

$$\frac{\partial \rho}{\partial t} + \nabla \cdot (\rho \mathbf{v}) = 0 \quad \text{Eq. 8a}$$

$$\frac{\partial}{\partial t}(\rho \mathbf{v}) + \nabla \cdot (\rho \mathbf{v}\mathbf{v}) = -\nabla p + \rho \mathbf{g} + \nabla \cdot (\mu \nabla \mathbf{v}) \quad \text{Eq. 8b}$$

$$\rho C_{\mathrm{p}} \frac{\partial T}{\partial t} + \rho C_{\mathrm{p}} \nabla \cdot (\mathbf{v} T) = \nabla \cdot (k \nabla T) \quad \text{Eq. 8c}$$

In the above equations, $\mathbf{v}$ is the velocity vector, p is the pressure and μ is the dynamic viscosity of the fluid. The assumption of a laminar flow regime is justified by the low Reynolds numbers calculated across the system; specifically, the maximum Reynolds number in the channels (the primary cooling contact area) is Re = 49, which is well below the critical threshold for internal flows. In the solid domains, (i.e. the rest of the solid components of the mechanic assembly, which is symbolized by subindex s), the energy equation is the following:

Table 3
Contact resistance in the union of different passive regions.

Contact surface	Resistance value [mΩ]
Terminal (+) – Busbar (+)	$5{\cdot}10^{-2}$
Terminal (−) – Busbar (−)	$5{\cdot}10^{-2}$
Busbar (−) – Tab (−)	$5{\cdot}10^{-2}$
Busbar (+) – Tab (+)	$7{\cdot}10^{-2}$
Busbar (//) – Tab (−)	$6{\cdot}10^{-2}$
Busbar (//) – Tab (+)	$7{\cdot}10^{-2}$

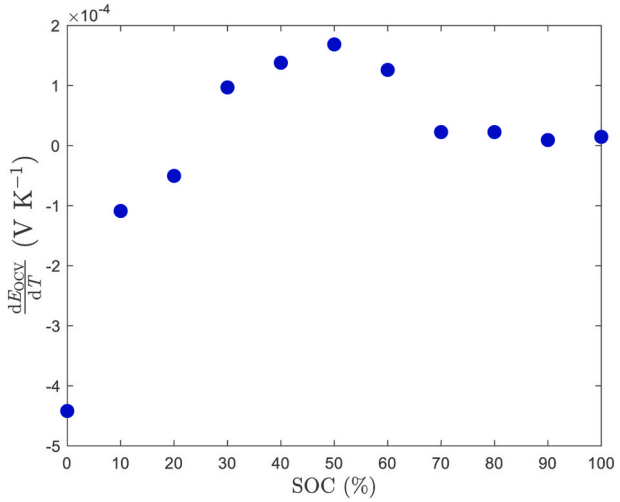

Fig. 4. Measured entropic factor values for different SOCs ($T = 25$ °C).

$$\rho_s C_{p,s} \frac{\partial T_s}{\partial t} = \nabla \cdot (k_s \nabla T_s). \qquad \text{Eq. 9}$$

3.3. Reduced Order Modelling (ROM)

The computational time and cost required to solve all the above equations in a transient framework is extremely large. Thus, to minimize the solver consumption, a particular procedure using a ROM technique is followed. This technique has been successfully applied in other battery models such as [39,40,51]. For this purpose, the following assumptions are considered [12]: (i) the flow behavior does not change with temperature, (ii) the electric conductivity of the cell is constant and does not vary with temperature, and (iii) the transfer current density is uniform in the active zone. First the flow governing equations (Eq. 8a-c) are only solved in a steady state framework. After that, considering the flow parameters constant (assumption i), the two potential equations are solved for initial time-steps until the current density and potential reach a steady value on each cell. Proper tuning of the convergence criteria is essential to guarantee the stable and accurate resolution of both potential equations. Once convergence is achieved, and under assumptions (ii) and (iii), the two equations reduce to homogeneous linear partial differential equations. Consequently, instead of solving them at each time step, a scaled solution procedure is employed to improve computational efficiency. This approach enables the potential fields corresponding to any electrical load to be derived from a reference potential field. This reference field is pre-calculated at reference load conditions, without needing to solve potential equations on each time-step. Thus, the ROM electrochemical-thermal coupled simulations are reduced to a pure thermal simulation under any current load (steady or transient), reducing significantly the computational cost of the model [51].

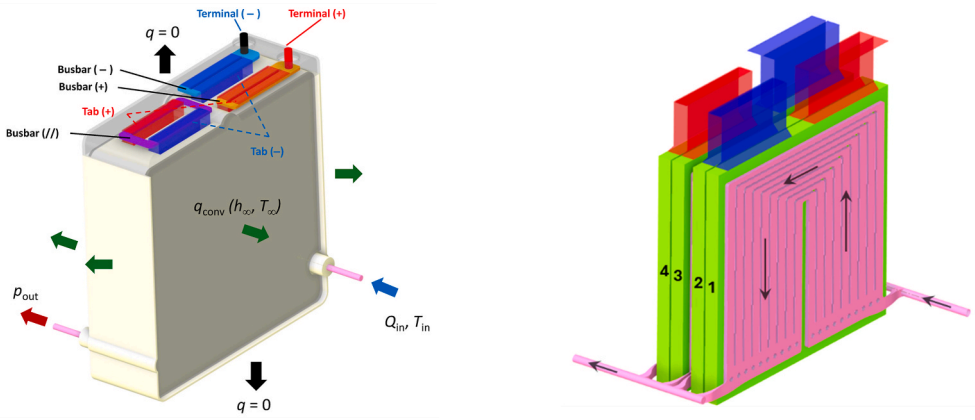

Fig. 5. Computational domain: (a) External, and (b) Internal view.

3.4. Computational domain and boundary conditions

Fig. 5 shows the (a) external and (b) internal view of the computational domain. The dielectric fluid enters the domain from the bottom left side to the interior of the module at specific temperature (T_{in}) and flow rate (Q_{in}), leaving it from the bottom-right zone (set as atmospheric pressure) of the system in a higher temperature due to the absorbed heat. As mentioned above, this heat is generated in both active (cells) and passive components (tabs, busbars and terminals).

In the present model the heat generated is also transferred to both the cooling fluid and through the vertical walls to the surrounding air. Therefore, as the experimental tests were carried out in a climatic chamber at $T_{\infty} = 25\ ^{\circ}C$, Newmann boundary condition (convective heat transfer) was set to the external faces. To consider the impact of the surface temperature on it, the convection coefficient was determined in terms of the wall surface temperature. To determine the convection coefficient (h_{∞}, W m^{-2} K^{-1}), the well-known correlation of Churchill and Chu for vertical plates was employed [52].

$$\mathrm{Nu} = \left\{ 0.825 + \frac{0.387\mathrm{Ra}_L^{1/6}}{\left[1 + (0.492/\mathrm{Pr})^{9/16}\right]^{8/27}} \right\}^2 = \frac{h_{\infty} L}{k}. \quad \text{Eq. 10}$$

Properties were determined for the average temperature $T_{avg} = T_w - T_{\infty}$, where T_w(K) is the temperature of the computational node located on the wall surface. Thus, by means of the values of Eq. (10), the fitted correlation of Eq. (11) was employed in the numerical model:

$$h_{\infty} = 8.00253 \cdot 10^{-4} T_w^3 - 7.43528 \cdot 10^{-1} T_w^2 - 2.30357 \cdot 10^{2} T_w + 2.37941 \cdot 10^{4}. \quad \text{Eq. 11}$$

Apart from that, since the module was leaning on a sheet of insulating material, the bottom surface was considered as adiabatic wall. In contrast, as the air surrounding passive electrical elements (terminals, busbars and tabs) are enclosed inside the module vessel, a constant convection coefficient $h_{passive} = 2$ W m^{-2} K^{-1} is imposed on these faces. This value was determined using the correlation for vertical rectangular enclosures proposed by Berkovsky and Polevikov [53].

4. Results and discussion

The results of the numerical model developed are presented below. First, the mesh independence analysis and the validation of the model are shown. Then, the thermal analysis of the system is deepened, focusing on the heat generation mechanisms and discussing the relevance of the contact resistances in the total heat generation. Finally, their effect on the magnitude and temperature distribution of the active parts of the module is analyzed and discussed.

4.1. Mesh independence analysis and model validation

First, the mesh independence analysis is conducted, which was validated using both experimental steady and transient pulse tests.

In the present study, Ansys Fluent Meshing was used to build the different meshes. As the aim of the numerical study is to analyze the thermal behavior of the cells including passive components (busbars, terminals and tabs) of the DLC technology, the influence of the mesh size on both passive components and fluid domain is studied. Four different grids are studied as follow: Mesh 1 $\approx 5.7 \times 10^6$ elements; Mesh 2 $\approx 7.5 \times 10^6$ elements; Mesh 3 $\approx 10.5 \times 10^6$ elements; and Mesh 4 $\approx 12.5 \times 10^6$ elements. Fig. 6 compares the

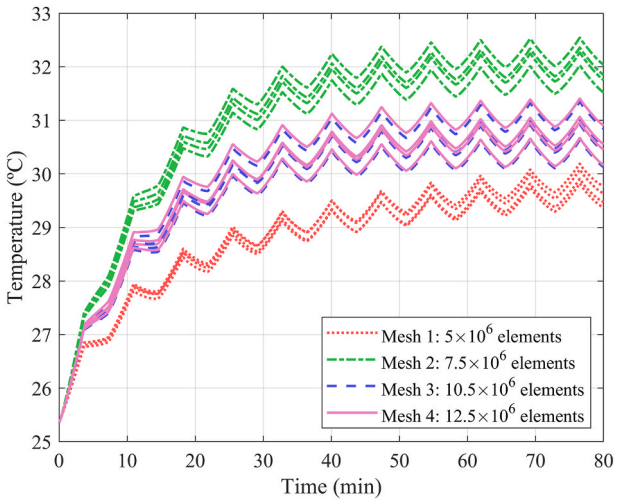

Fig. 6. Average temperature of each cell over time for four different meshes.

evolution of the average temperature of the four cells for different meshes under 1.5C pulse test conditions (see Fig. 2a) with ambient and inlet fluid temperatures of 25 °C.

Results show that the thermal behavior of the Mesh 3 and Mesh 4 converge to similar values. Thus, to have a good compromise between a reduced computational cost and numerical accuracy, a grid of 10.5×10^6 elements was selected, having the following main characteristics: maximum size on busbars, terminals and tabs of 4×10^{-4} m, maximum size on the fluid domain of 6×10^{-4} m, minimum of 10 elements on the transversal direction of the fluid domain and a maximum size on the rest of the components of 8×10^{-3} m.

After ensuring the mesh independence of the numerical results, the model was validated against experimental data. Furthermore, in order to validate the numerical model over a wide range of inlet flows, the model was simulated under the same electrical (1.5C pulse test) and thermal operating conditions (ambient and inlet fluid temperatures of 25 °C) with three different cooling fluid flow rates: 0.3 L/min, 0.9 L/min and 1.5 L/min. Fig. 7, compares the evolution of the experimental and numerical minimum, mean and maximum temperatures of the battery module for the different considered inlet flow rates.

As can be concluded from Fig. 7, the numerical model correctly characterizes the thermal behavior of the tested module throughout the full range of simulated flow rates. In addition to correctly capturing the magnitude and dispersion of the stationary temperatures of the battery module after applying 1.5C pulses for around 70 min, the transient evolution of the temperatures is also accurately captured. For all flow rate values, the minimum, mean and maximum temperature of the module is determined with an error below 1 °C. The difference between the maximum and minimum temperature is correctly captured although the errors become larger as the volumetric flow rate of the liquid increases. In addition, to further support the validation, the spatial distribution of the steady-state temperature for internal and external cells was compared. Fig. 8 shows the experimental and numerical temperature contours for external (cell 1) and internal cells (cell 3) operating under different coolant flow rates. The stationary conditions reached at the end of the pulse test ($t = 71$ min) were considered for this purpose.

The numerical model is thus validated as accurately representing both transient and steady-state temperature profiles of the module. Furthermore, it successfully reproduces the spatial temperature distribution across cells located at the center and sides of the module under varying coolant inflow conditions, when subjected to 1.5C pulses between 50% and 60% SOC.

In order to finish the validation, the numerical model was also used to calculate the thermal response of the module under a real driving cycle. The driving cycle includes a fast charge of 1.6C, in which higher heat generation is expected to impact both the mean temperature value as well as the spatial homogeneity of the temperature. The measured and computed thermal responses are represented in Fig. 9 for an external (cell 1) and an internal cell (cell 3).

As can be seen in Fig. 9, the numerical model correctly represents the overall thermal response of the cells throughout the driving cycle. Regarding the most demanding phase, the initial stage of fast charging is accurately captured by the model. However, discrepancies are observed during the final phase, particularly between SOC values of 60 % and 90 %. These deviations are consistent with three coupled mechanisms that are not fully represented in the present parameterization.

First, the temperature-dependent of contact resistance in the union of different passive regions. Electrical interconnects can contribute non-negligible Joule heating when contact resistance increases with temperature; this is well documented for tab-to-busbar welds, and has been shown to produce localized hot spots under high-current operation [54]. Neglecting the temperature rise of contact resistance may therefore underpredict heat generation near the tabs at high SOC and towards the end of fast charging.

Second, possible underestimation of the reversible heat at elevated SOC. The reversible or entropic heat term becomes increasingly relevant at high SOC in NMC chemistries. Literature emphasizes that accurate characterization of the entropic factor across SOC—ideally via multi-temperature OCV–standby protocols—is required to avoid bias in the entropic contribution during fast charging [55]. While our coefficients were experimentally determined at 25 °C (see Fig. 4), small underestimation at SOC >60 % would directly translate into lower predicted heat generation and premature saturation of the simulated peak temperature.

Third, pressure-dependent impedance rises due to swelling at high SOC and temperature. Pouch cells experience swelling that elevates stack pressure; multiple studies link pressure increases and pressure gradients to impedance rise and polarization growth, especially under high C-rates and elevated temperatures [56,57]. Such electro-chemo-mechanical coupling can sustain higher experimental temperatures and delay their decay after current reduction, producing precisely the lag observed in Fig. 9.

It is important to note that each of the aforementioned mechanisms would require dedicated electro-chemo-mechanical

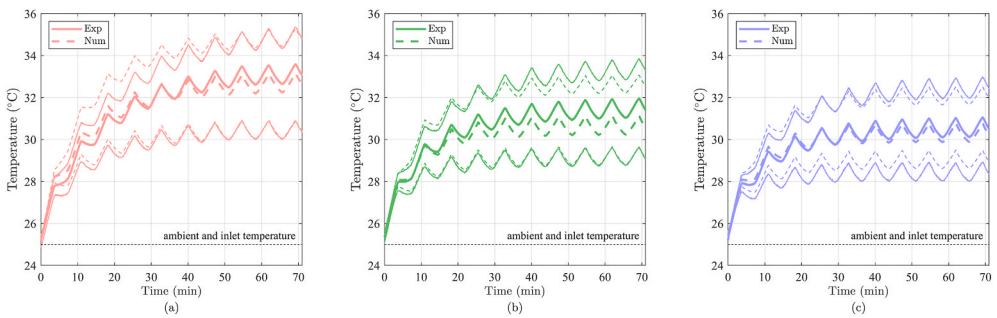

Fig. 7. Experimental and numerical evolution of the minimum, average and maximum temperatures of the battery module under 1.5C pulse tests with ambient and inlet fluid temperatures of 25 °C, and different volumetric flow rates: (a) 0.3 L/min; (b) 0.9 L/min; (c) 1.5 L/min.

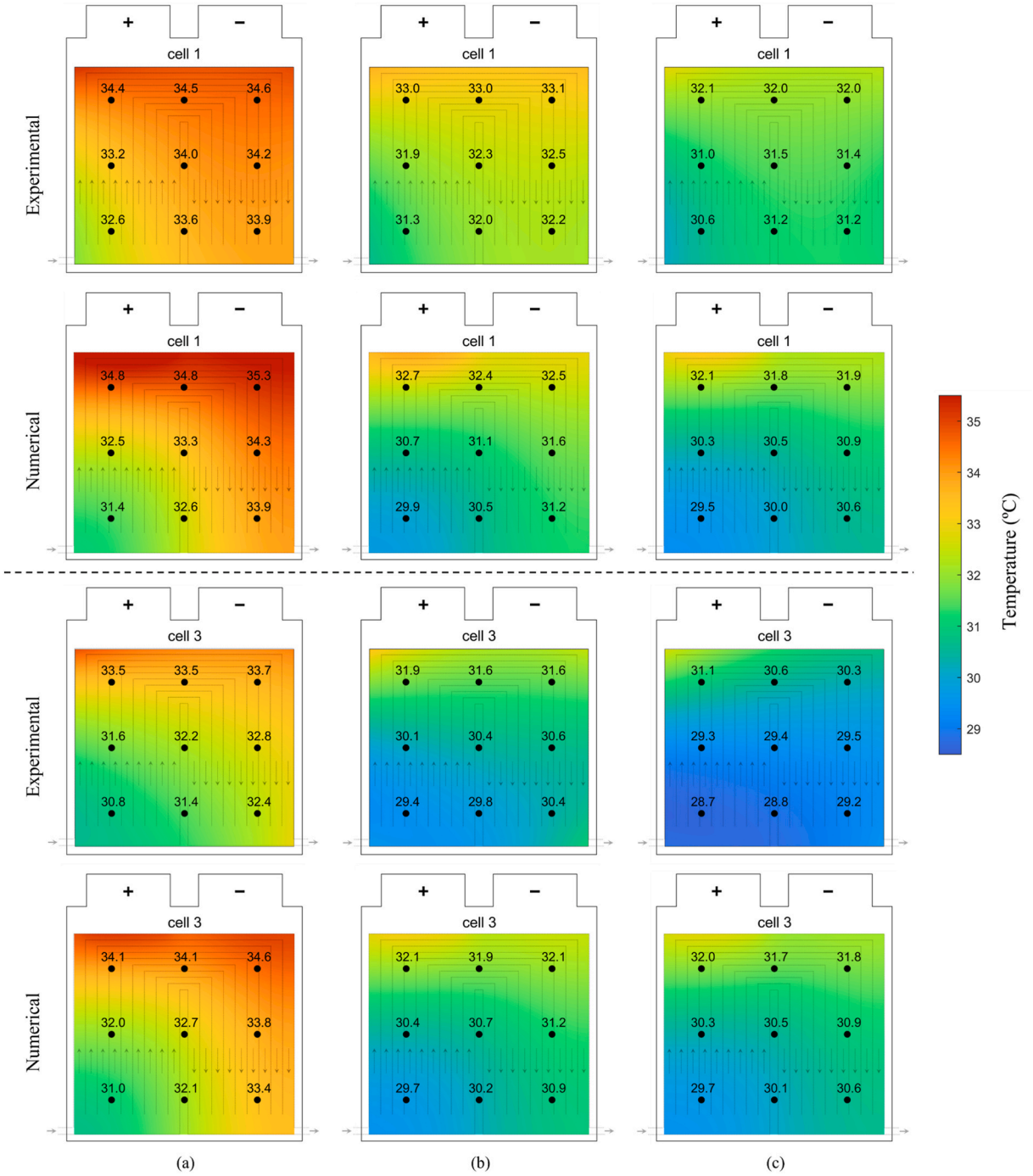

Fig. 8. Experimental and numerical steady-state temperature contours of Cell 1 (external cell) and Cell 3 (internal cell) with 0.3 L/min, 0.9 L/min and 1.5 L/min cooling fluid flowrates under 1.5C pulses with 25 °C fluid inlet and ambient temperature.

characterization to be fully represented in a predictive model. Such comprehensive modelling lies beyond the scope of the present study, whose primary objective is to quantify the influence of contact resistances under experimentally validated thermal–fluidic conditions. For this reason, and to ensure that the contact-resistance analysis is grounded in fully validated scenarios, the final section of the paper compares the effect of modifying the contact resistances on the system temperature under steady-state operating conditions. This approach ensures that the comparison between simulations with and without contact resistance is performed in a regime where the model accuracy has already been independently verified, thereby strengthening the robustness and interpretability of the resulting conclusions.

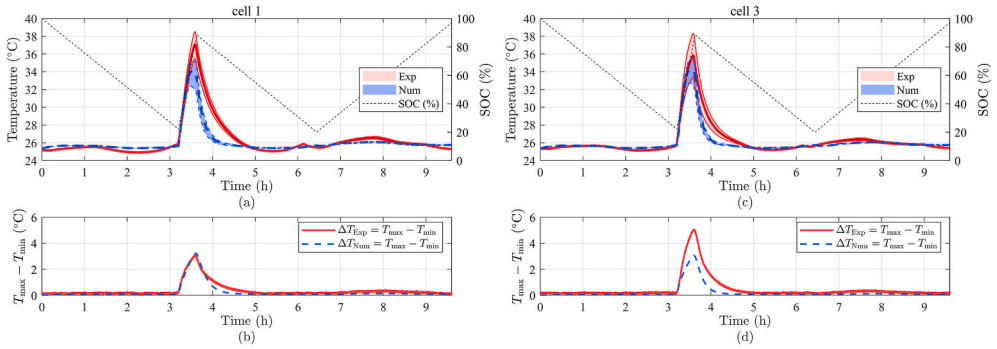

Fig. 9. Experimental and numerical thermal responses of the external cell 1 and the internal cell 3 under a real driving cycle. (a, c) Evolution of the minimum, mean and maximum temperature of the cells. (b, d) Difference between the maximum and minimum temperature of the cells.

4.2. Thermal analysis

After validating the numerical model, the thermal behavior of the pouch-module is studied. For this purpose, Fig. 10 shows the thermal behavior of the active and passive components for the steady (Fig. 10a) and transient conditions (Fig. 10b). As in the validation case, the thermal maps of the steady state case correspond to the final instant, while for the transient case they coincide with the end of the 1.6C semi-fast charge (90 % SOC).

The results depict that in both cases the temperature distribution of the components is qualitatively very similar. However, what stands out in the figures is that the temperatures at the end of the semi-fast profile reach to a slightly superior values (Fig. 10b). Moreover, both figures postulate that the temperatures of the passive components are significantly higher. In particular, the maximum temperature resides near the positive terminal. This behavior should be attributed to different aspects. On the one hand, the cooling

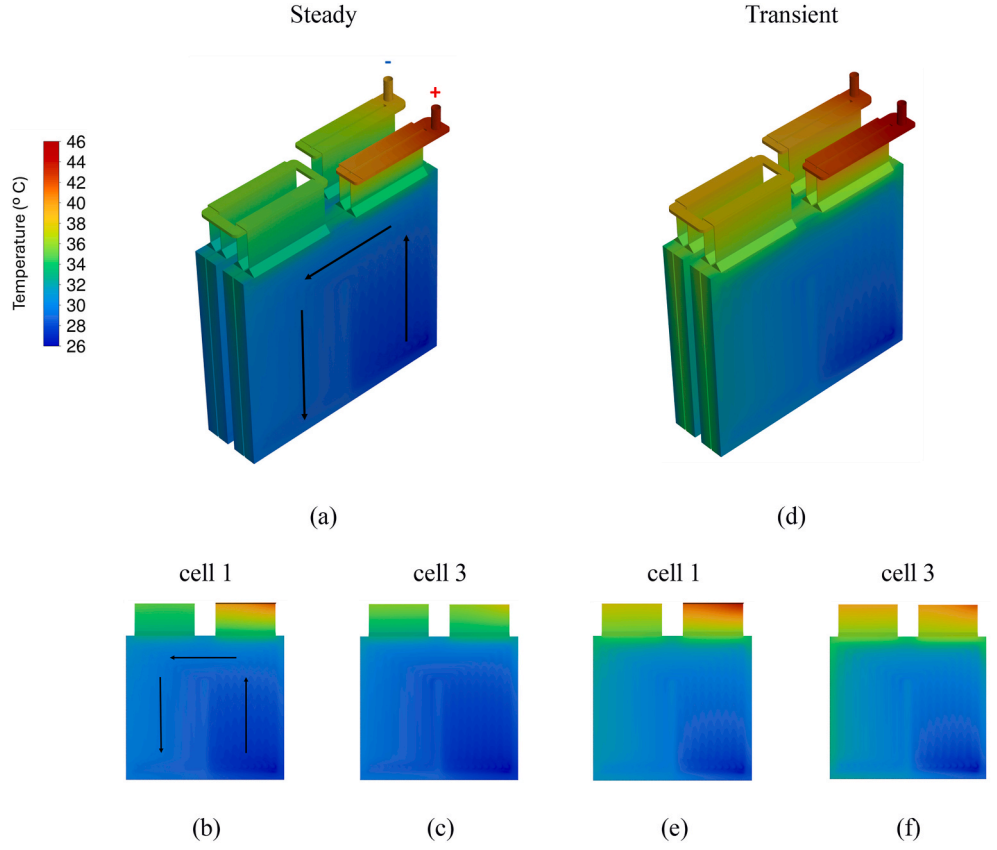

Fig. 10. Surface temperature distribution for steady pulses (a, b, c) and transient profile at the end of the semi-fast charging region (d, e, f); (a, d) Battery module, (b, e) cell 1, (e, f) cell 3.

fluid is only in contact with the active elements (cells) of the module, so the passive components are only refrigerated via the enclosed air. On the other hand, the high current carried through the terminals, together with the heat generated at the contact region between the terminals and the busbars, should also cause the temperature increase. In addition to the cooling and contact-resistance mechanisms discussed above, it is also worth noting that the hottest spot consistently appears near the positive terminal due to the intrinsic asymmetry between the two tab materials. In these cells, the positive tab is made of aluminum, whereas the negative tab is copper. Since aluminum presents lower electrical and thermal conductivity than copper, the positive side naturally exhibits higher ohmic losses and reduced ability to dissipate heat. This material-driven imbalance increases the effective contact resistance around the positive terminal, amplifying the local Joule heating. This phenomenon will be studied in more detail in Sections 4.3 and 4.4.

As in Section 4.1, the temperature distribution of the cell surface is also analyzed. Figs. 10b and c illustrate the thermal map of cell 1 and cell 3 for the steady pulse profile, respectively, whereas Figs. 10e and f provide for the transient profile. It should be noted that the showed temperature maps are those that are in contact with the dielectric fluid, whereas the maps in Fig. 8 showed the cell temperature on the surface opposite to that contacted by the liquid, hence they are inverted on the vertical axis. Like in the battery module, both cases are qualitatively very comparable, achieving slightly superior temperatures in the transient one. Analyzing in detail the cell thermal maps, results show that the cooling flow direction affects the temperature. Therefore, in general, the temperature is higher downstream. Nevertheless, the most interesting aspect is the superior temperature of the more elevated zones of the cells that are closest to passive components. Temperature maps show that the hottest spot corresponds to the tab in contact with the positive terminal. Therefore, the thermal non-uniformity does not only occur due to the warming of the dielectric fluid, but also due to the heat generated in the passive components (namely conductive joule heat) and in their contact zones (hereafter referred to as contact resistance heat, or CR heat). Therefore, these results suggest that the ohmic heat could have a significant influence on both the value and non-uniformity of the temperature of immersion cooling pouch-type battery modules specially under high charge/discharge rates. Thus, the weight and impact of this heat will be analyzed in Section 4.3.

4.3. Heat generation analysis

To quantify the impact of the heat generated in the passive components, the different heat generation sources within the battery module were evaluated. By means of the previously validated numerical model, it has been possible to break down the total heat generation considering the electrochemical heat of the active zones (irreversible heat generation, and the reversible or entropic heat generation) and the ohmic heat of the passive zones heat (conductive joule heat and the CR heat) during the charging and discharging phases.

To understand the meaning of the different heat sources, first they are defined. The total generated heat is the sum of all heat sources within the module. In other words, it is the sum of the total electrochemical heat of the cells ($\dot{q}_{\mathrm{ECh}}$ of Eq. (1)) and the total ohmic heat of the passive zones (first two terms of the right hand of Eq. (1)). In particular, the electrochemical heat integrates the irreversible and reversible heats (first and second terms of right hand in Eq. (7), respectively). Fig. 11 presents the evolution of the different heat sources for the steady-state profile. In particular, it presents the profile of a single 1.5C charge and discharge cycle between 50 % and 60 % SOC, with a total duration of 8 min.

Results show that the total heat generated (black line) changes slightly with SOC, and significantly between charging and discharging phases. In contrast, the ohmic heat (orange line) is constant throughout the entire range, since this phenomenon does not depend on whether charging or discharging is performed. Therefore, the fall in the total heat generation should be due to the decrease of the electrochemical heat (blue line). Focusing on the irreversible heat, it can be observed that it changes with SOC and there is a not negligible reduction in the electrical current direction change instant. Nevertheless, what is interesting in this chart is the fall in the entropic heat at the same point. In the analyzed SOC range, the entropic factor (red dots) is positive. This means that during the

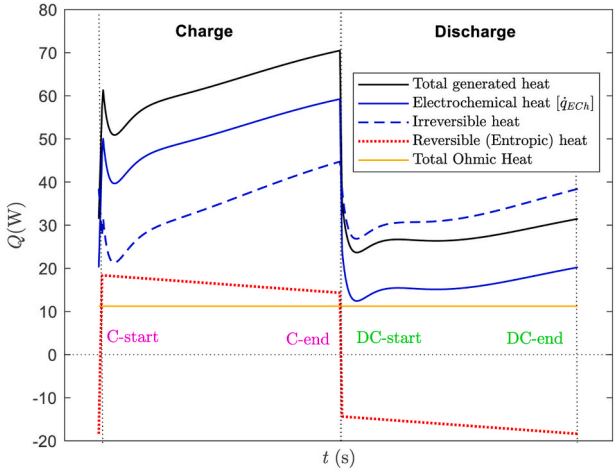

Fig. 11. Different heat generation sources within the module on a single cycle of the steady state pulse profile.

charging phase, the entropic heat reaction is exothermic, whereas it is endothermic during the discharging phase. Consequently, this phenomenon causes the drop in total generated heat. Furthermore, these results show that the impact of the ohmic source on the total heat changes significantly within the cycle, being higher within the discharge rate region.

In contrast, these great changes are not observed in the transient profile case. Fig. 12a presents the aforementioned heat sources for the real profile of electrical buses, while Fig. 12b shows only the region of the 1.6C semi-fast charge.

Out of battery semi-fast charging zone, the total heat generated is very small (even endothermic, Fig. 12a). In contrast, the heat generated presents a sharp increase in the semi-fast charge region. Locally examining Fig. 12b, the total heat changes with SOC. In particular, the total heat generated (black line) increases between 20 and 60 % SOC, and after that it presents a reduction. This trend can be explained by the combined evolution of irreversible and reversible heat. Reversible contribution is directly governed by the entropic factor, which remains positive throughout this SOC range. A positive entropic coefficient implies that the open-circuit voltage increases with temperature; therefore, during charge, the reversible term is exothermic. As SOC rises above 60 %, the experimentally determined entropic factor decreases in magnitude, reducing the reversible heat contribution. At the same time, the irreversible heat also decreases due to the reduction of overpotentials at high SOC. The combination of both effects leads to the observed drop in total heat generation. Therefore, as in the semi-fast charge region the ohmic heat also remains constant, its relative impact is higher in the beginning and end periods of the charge.

It is also worth noting that the entropic factors experimentally obtained in this work are slightly lower at high SOC compared with some values reported in the literature for NMC-based chemistries, where the entropic coefficient often shows a stronger positive peak around mid-SOC before decreasing more gradually at high SOC [55]. This difference may partially explain the reduced reversible heat contribution predicted numerically at SOC beyond 60 %, and is consistent with the tendency of our model to underestimate cell temperature during the final stage of fast charging.

Together, steady and transient results provide important insights into the effect that could have the ohmic heat on the total heat source. To certified this influence, Fig. 13 presents the ohmic heat ratio for both steady-state pulse (Fig. 13a) and semi-fast charge (Fig. 13b) profiles. This ratio is defined as the proportion between the total ohmic heat of the passive components and the total heat generated in the battery module. As it can be observed in Fig. 13, the profile of both cases is very different.

On the one hand, the influence of the ohmic heat changes with SOC in the steady state pulse profile (Fig. 13a). In addition, results show a sharp raise of the ratio due to reversible heat drop in the rate change zone. What stands out in the figure is the remarkable weight of the ohmic heat in some zones. The ohmic heat ratio could rise up to 46 % at the beginning of the discharge. Apart from that, its influence does not decrease below 16 %. On the other hand, Fig. 13b presents the semi-fast charge results. There is a great decrease at the beginning and after that the changes of the ratio are smoother. Interestingly, the average ratio of the ohmic heat in the semi-fast charge region is 17.5 %. These values correspond to our specific module design, cell chemistry, and operating conditions; extrapolation to other systems should be done cautiously.

Thus, the results of the ratio indicate that the heat generated in the passive components has a significant influence on the total heat generated, and therefore, on the thermal behavior of the battery module. Consequently, this ohmic heat contribution should be included in the numerical model to obtain accurate predictions of the thermal distribution within the battery module. It is important to note that the high ohmic heat ratios observed in this study are specific to the tested module configuration and operating conditions. While they highlight the significant thermal impact of passive components, caution should be exercised when extrapolating these ratios to other battery formats, cooling strategies, or load profiles.

As it was stated in the Introduction, one of the principal novelties of the numerical model of the present study is the consideration of the heat due to contact resistances between the passive components. This heat, together with the conductive joule heat due to the intrinsic electrical resistivity of the different components, integers the total ohmic heat. To analyze the impact of the CR heat, Fig. 14 depicts the percentage of each resistance over the total ohmic for the steady state pulse profile. Interestingly, more than two thirds of the total ohmic heat are due to the heat generated in the CR, stablishing the importance of this heat source. For example, the average influence of the CR heat can be determined for the semi-fast charging region. Considering an average ohmic ratio of 17.5 % previously

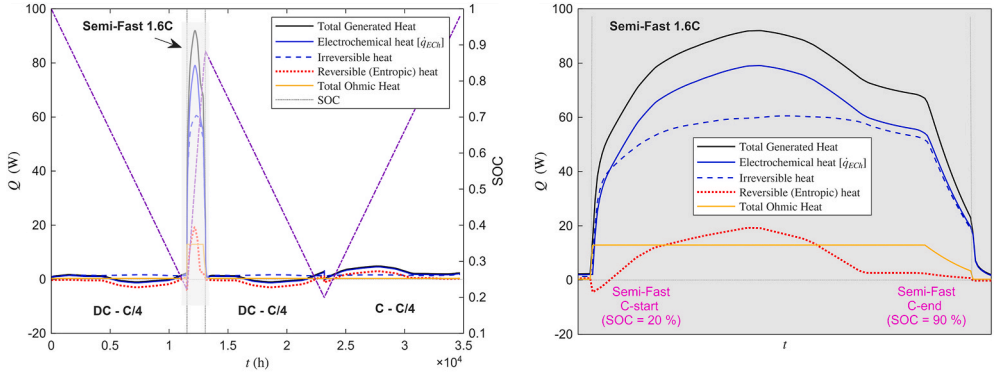

Fig. 12. Different heat generation sources within the module in the transient profile: (a) Entire test (b) 1.6C Semi-fast charge region.

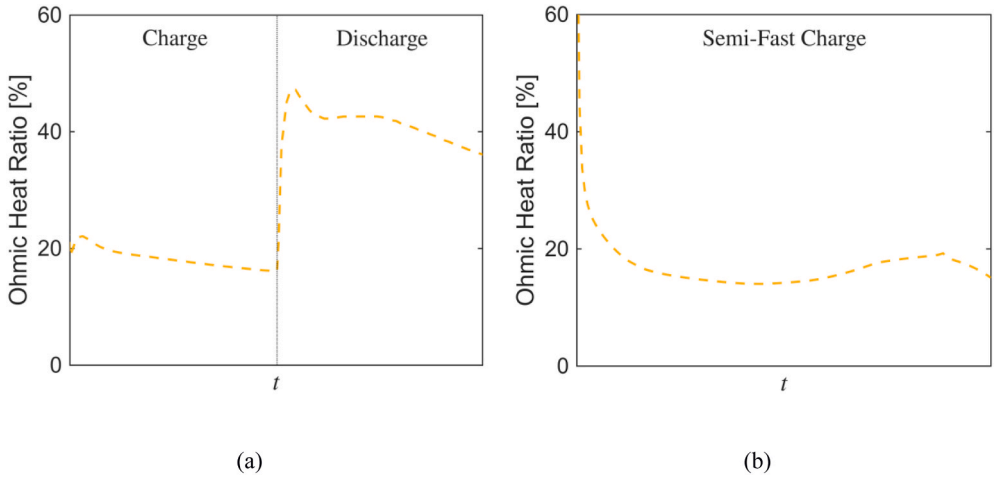

Fig. 13. Ohmic heat ratio on (a) a single cycle of the steady state pulse profile (b) 1.6C semi-fast charge region.

mentioned, the weight of the contact heat resistance reaches up to 12.2 % of the total generated heat in the semi-fast charging.

In the case of the present battery module, the contact resistances are located on the surfaces between each terminal and their corresponding busbar (Terminal — Busbar), between the parallelization busbar (Busbar (//)) and the positive and negative tabs (Tab (+) and Tab (−)) and between the positive and negative busbars (Busbar (+) and Busbar (−)) and their respective tabs (Tab (+) and Tab (−)) (see Fig. 5). Results reveal that the highest heat generation, driven by the conducted high current, is located in both parallelization busbar contacts, and on the surfaces between the terminal and their busbars. In contrast, as the current is divided throughout two cells in the other busbars, the heat generated on the contact with their cells tabs is significantly lower. Thus, the enhancement of the contact resistance of the terminals and the parallel busbar could improve the thermal performance of the battery module.

In summary, these results reinforce the need to consider the ohmic heat (and, mainly, the CR heat) to properly model and get accurate thermal results of pouch-type battery modules cooled by immersion cooling strategy at high rates. Likewise, the reduction of these CR would decrease the total generated heat and, as a result, would reduce the maximum temperature, as well as the non-uniformity of the cells themselves. The next section, therefore, moves on the discussion of this effect.

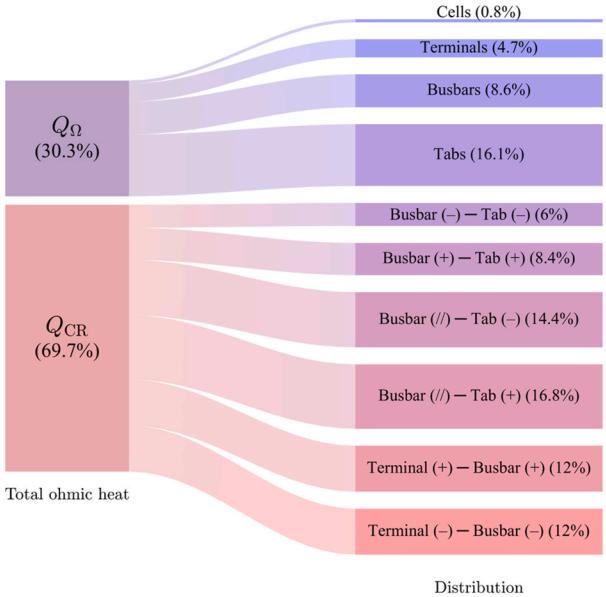

Fig. 14. Percentage of the conductive joule heat (Q_Ω) and the contact resistance heat (Q_{CR}) over total ohmic heat, and a breakdown of each one, indicating the percentage of the heat in each location for the conductive heat, and the percentage of the heat generated in each contact between passive elements (terminals, busbars and tabs). Both are determined for the steady state pulse profile.

4.4. Contact resistance influence

To study the impact of the heat generated due to the contact resistances in more detail, a new model with null CR was built. Therefore, the aforementioned CR heats were not considered in the present case. In this occasion both steady and transient cases are analyzed. To evaluate the effect in the thermal performance of the battery module, Table 4 provides the overall results of the battery cells at the end of both steady state pulse profile and the semi-fast 1.6C charge region for the studied cases: with and without considering CR heat.

It is apparent from Table 4 that the CR has a significant influence on the thermal performance of the cells, mainly on the maximum temperature and the temperature non-uniformity ($\Delta T = T_{max}$ - T_{min}) within the cells. This influence is higher for the semifast charge case. It is worth noting that the maximum temperature decreased by 2.8 and 4.9 °C after removing the heat contribution from the contacts, also leading to an improvement in temperature homogeneity. Despite being less significant, the average temperature of the active components also dropped by 0.6 and 1.5 °C, respectively. Finally, it should be noted that the temperature difference between the maximum and minimum values was reduced by 2.8 °C and 4.8 °C, respectively, which represents a reduction of more than half in the semi-fast charge case.

To further study this impact, Fig. 15 shows the thermal maps of both cases for the steady-state profile. In particular, Fig. 15a illustrates the surface temperature of the module components neglecting the CR, while Figs. 15b and c show the temperature difference when considering and not considering the CR for the external (cell 1) and the internal cells (cell 3), respectively. Compared to the CR case (Fig. 10d), it is apparent that the achieved temperature in the module is considerably lower. This reduction is more significant among the passive components. Analyzing the temperature differences in the cells 1 and 3, results show that the impact is more pronounced in the upper 25 % area, close to the passive components. Interestingly, in this region the temperature rise due to the contact resistance can range from 1.5 °C to 3.0 °C. In this case, the most influenced zone is located on the zone below the positive terminal. In contrast, in the rest of the surface the impact is lower, being almost negligible on the bottom part as heat transfer is dominated by convection to the liquid wetting the face.

In summary, these results indicate the significant impact of the heat generated in the contact between the passive components. Therefore, they suggest that the contact resistance should be considered to properly model the thermal performance of pouch-type battery modules working at high rates. Otherwise, the achieved temperature maps will not show the real thermal distribution of the module. Furthermore, this heat should be also contemplated to understand the results of the experimental studies, as they distort the temperature uniformity along the cells surface themselves. So, taken together, these findings also indicate that the reduction of the contact resistance may be a key solution for improving the temperature performance of the battery modules. By applying this approach, temperature homogeneity among the active components would be reduced, while also decreasing the overall temperature of the cell.

5. Conclusions

This study presents a validated numerical model of a pouch-type lithium-ion battery module cooled via a partial direct liquid cooling (DLC) strategy. The model incorporates both electrochemical and ohmic heat sources, including contact resistance (CR) effects between passive components—an aspect rarely addressed in previous literature.

The model was validated against our own experimental data under both steady-state and transient conditions, and across a wide range of coolant flow rates. Importantly, validation was not limited to average cell temperatures, but extended to spatial temperature distributions, allowing the assessment of thermal non-uniformity within and between cells. The model accurately reproduced the thermal behavior of the module, with prediction errors below 1 °C for the steady state pulse profile.

Results show that under high C-rate conditions (1.5C discharge and 1.6C semi-fast charge), ohmic heating can account for up to 46 % of total heat generation, with CR heat contributing up to 12.2 %. These values are specific to the tested configuration and operating conditions and should not be generalized without further investigation. Nonetheless, they highlight the significant thermal impact of passive components and the necessity of including them in thermal models.

Small discrepancies between simulation and experiment were observed during the final stage of fast charging, particularly in regions close to busbars, tabs, and other passive components. The analysis indicates that these deviations stem from the combined influence of mechanisms not yet fully captured in the present model—namely, the temperature-dependent increase in contact resistances, a possible underestimation of the reversible heat at high SOC, and swelling-induced impedance rise under elevated temperature and state of charge.

Overall, the proposed model provides a robust framework for analyzing the thermal behavior of pouch-cell battery modules under demanding conditions. Although the numerical values reported here are specific to the studied configuration, the methodology is fully generalizable to other module layouts, cell formats and electrical topologies. Moreover, the modeling strategy offers a solid basis for extending the analysis to more severe thermal scenarios—such as thermal-runaway initiation and propagation—and constitutes a valuable design tool for assessing alternative geometries, welding processes and contact-interface configurations aimed at minimizing thermal gradients and contact-resistance effects.

CRediT authorship contribution statement

P.F. Arroiabe: Writing – original draft, Validation, Investigation, Data curation, Conceptualization. **J. Berasategi:** Writing – review & editing, Supervision, Investigation, Conceptualization. **M. Larrañaga-Ezeiza:** Writing – review & editing, Validation,

Table 4
Overall temperature results for the active components (cells) of the battery module with (CR Heat) and without (No CR Heat) considering the contact resistance.

	Case	T_{avg} (°C)	T_{max} (°C)	ΔT (°C)
Steady-state profile	CR Heat	30.5	34.0	7.7
	No CR Heat	29.9	31.2	4.9
Semi-Fast charging	CR Heat	30.8	36.0	9.3
	No CR Heat	29.3	31.1	4.5

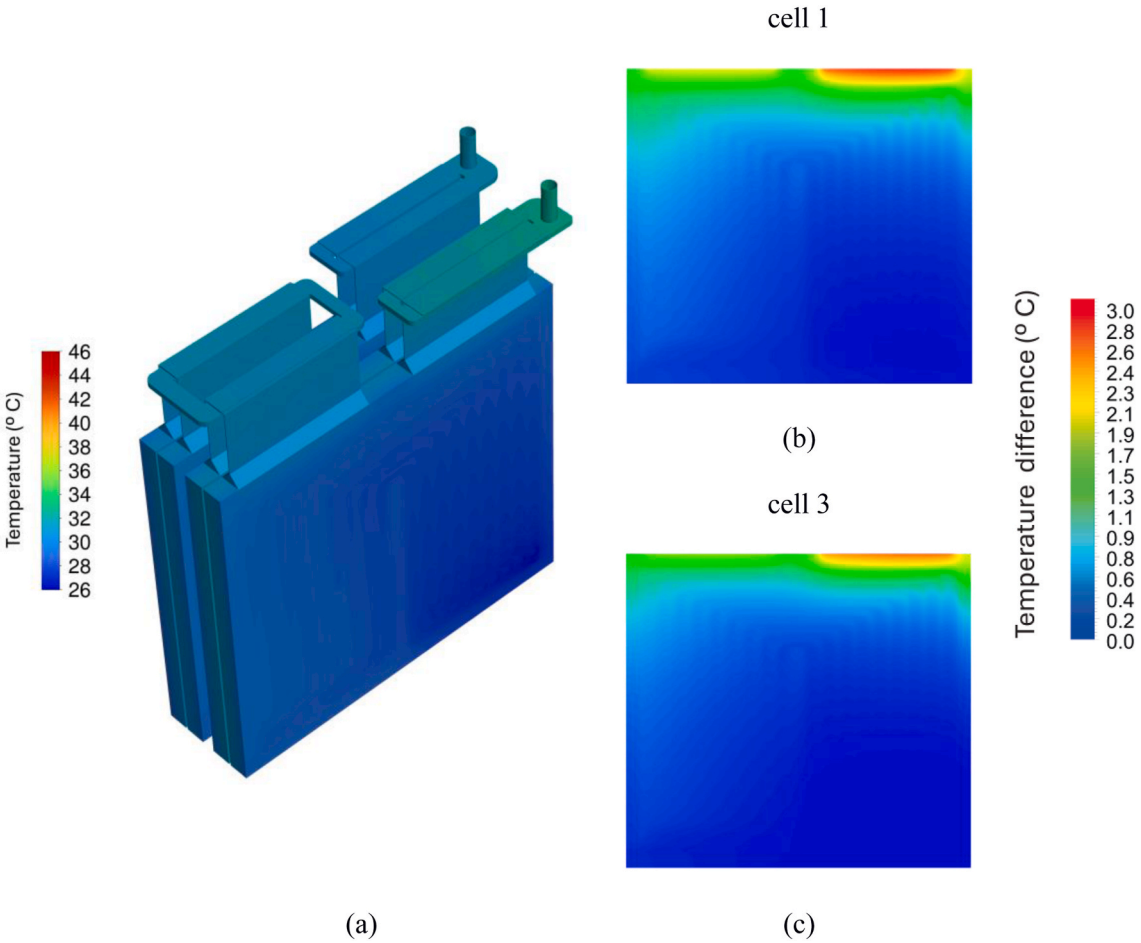

Fig. 15. (a) Battery surface temperature distribution neglecting the CR heat for the steady state profile. Difference on the surface temperature with and without considering the contact resistance for (b) external cell1, and (c) internal cell 3.

Investigation, Data curation. **G. Vertiz:** Supervision, Investigation, Funding acquisition, Conceptualization. **I. Galarza:** Validation, Investigation, Data curation. **M. Martinez-Agirre:** Writing – review & editing, Visualization, Supervision, Funding acquisition, Conceptualization.

Declaration of competing interest

The authors declare the following financial interests/personal relationships which may be considered as potential competing interests:P.F. Arroiabe reports financial support was provided by Basque Government. J. Berasategi reports financial support was provided by Basque Government. M. Larranaga-Ezeiza reports financial support was provided by Basque Government. G. Vertiz reports financial support was provided by Basque Government. I. Galarza reports financial support was provided by Basque Government. M. Martinez-Agirre reports financial support was provided by Basque Government. If there are other authors, they declare that they have no known competing financial interests or personal relationships that could have appeared to influence the work reported in this paper.

Acknowledgments

All the authors acknowledge the financial support from the Basque Government under the BAT4ME25 project (KK-2025/00094 Elkartek program). P.F.A, M.M-A and J.B would like to thank the financial support from the Basque Government under Research Group Program (IT1505-22).

Data availability

Data will be made available on request.

References

[1] E. Parliament, EU ban on the sale of new petrol and diesel cars from 2035 explained, (n.d.). https://www.europarl.europa.eu/news/en/headlines/economy/20221019STO44572/eu-ban-on-sale-of-new-petrol-and-diesel-cars-from-2035-explained.
[2] E.C.-C. of the European Union, Fit for 55, (n.d.). https://www.consilium.europa.eu/en/policies/green-deal/fit-for-55-the-eu-plan-for-a-green-transition/.
[3] E. Commission, A European green deal, (n.d.). https://commission.europa.eu/strategy-and-policy/priorities-2019-2024/european-green-deal_en.
[4] V.G. Choudhari, D.A.S. Dhoble, T.M. Sathe, A review on effect of heat generation and various thermal management systems for lithium ion battery used for electric vehicle, J. Energy Storage 32 (2020) 101729, https://doi.org/10.1016/j.est.2020.101729.
[5] L. Lu, X. Han, J. Li, J. Hua, M. Ouyang, A review on the key issues for lithium-ion battery management in electric vehicles, J. Power Sources 226 (2013) 272–288, https://doi.org/10.1016/j.jpowsour.2012.10.060.
[6] A. Väyrynen, J. Salminen, Lithium ion battery production, J. Chem. Thermodyn. 46 (2012) 80–85, https://doi.org/10.1016/j.jct.2011.09.005.
[7] A. Wahab, A.U.H. Najmi, H. Senobar, N. Amjady, H. Kemper, H. Khayyam, Immersion cooling innovations and critical hurdles in Li-ion battery cooling for future electric vehicles, Renew. Sustain. Energy Rev. 211 (2025), https://doi.org/10.1016/j.rser.2024.115268.
[8] Manisha, S. Tiwari, R.K. Sahdev, D. Chhabra, M. Kumari, A. Ali, R. Sehrawat, P. Tiwari, Advancements and challenges in battery thermal management for electric vehicles, Renew. Sustain. Energy Rev. 209 (2025), https://doi.org/10.1016/j.rser.2024.115089.
[9] C. Roe, X. Feng, G. White, R. Li, H. Wang, X. Rui, C. Li, F. Zhang, V. Null, M. Parkes, Y. Patel, Y. Wang, H. Wang, M. Ouyang, G. Offer, B. Wu, Immersion cooling for lithium-ion batteries – a review, J. Power Sources 525 (2022), https://doi.org/10.1016/j.jpowsour.2022.231094.
[10] A. Celen, Experimental investigation on single-phase immersion cooling of a lithium-ion pouch-type battery under various operating conditions, Appl. Sci. 13 (2023), https://doi.org/10.3390/app13052775.
[11] M. Suresh Patil, J.H. Seo, M.Y. Lee, A novel dielectric fluid immersion cooling technology for Li-ion battery thermal management, Energy Convers. Manag. 229 (2021), https://doi.org/10.1016/j.enconman.2020.113715.
[12] A. Verma, T. Saikia, P. Saikia, D. Rakshit, C.E. Ugalde-Loo, Thermal performance analysis and experimental verification of lithium-ion batteries for electric vehicle applications through optimized inclined mini-channels, Appl. Energy 335 (2023), https://doi.org/10.1016/j.apenergy.2023.120743.
[13] M. Larrañaga-Ezeiza, G. Vertiz, P.F. Arroiabe, M. Martinez-Agirre, J. Berasategi, A novel direct liquid cooling strategy for electric vehicles focused on pouch type battery cells, Appl. Therm. Eng. (2022) 118869, https://doi.org/10.1016/j.applthermaleng.2022.118869.
[14] Y. Wang, C. Li, X. Wen, W. Cai, Y. Jiang, C. Wen, Y. Wang, L. Hu, H. Yu, H. Zhu, H. Guo, D. Liu, Experimental studies on two-phase immersion liquid cooling for Li-ion battery thermal management, J. Energy Storage 72 (2023), https://doi.org/10.1016/j.est.2023.108748.
[15] Y. Li, M. Bai, Z. Zhou, W.T. Wu, J. Lv, L. Gao, H. Huang, Y. Li, Y. Song, Experimental studies of reciprocating liquid immersion cooling for 18650 lithium-ion battery under fast charging conditions, J. Energy Storage 64 (2023), https://doi.org/10.1016/j.est.2023.107177.
[16] L. Giammichele, V. D'Alessandro, M. Falone, R. Ricci, Experimental study of a direct immersion liquid cooling of a Li-Ion battery for electric vehicles applications, Int. J. Heat Technol. 40 (2022) 1–8, https://doi.org/10.18280/ijht.400101.
[17] L. Giammichele, V. D'Alessandro, M. Falone, R. Ricci, Preliminary analysis of a novel battery thermal management system based on a low boiling dielectric fluid, in: IOP Conf. Ser. Earth Environ. Sci., Institute of Physics, 2022, https://doi.org/10.1088/1755-1315/1106/1/012017.
[18] N.P. Williams, S.M. O'Shaughnessy, Immersion cooling of lithium-ion batteries for electric vehicles, in: 2022 28th International Workshop on Thermal Investigations of Ics and Systems (THERMINIC), 2022, pp. 1–4, https://doi.org/10.1109/THERMINIC57263.2022.9950646.
[19] M. Luo, J. Cao, N. Liu, Z. Zhang, X. Fang, Experimental and simulative investigations on a water immersion cooling system for cylindrical battery cells, Front. Energy Res. 10 (2022), https://doi.org/10.3389/fenrg.2022.803882.
[20] Q. Liu, C. Sun, J. Zhang, Q. Shi, K. Li, B. Yu, C. Xu, X. Ju, The electro-thermal equalization behaviors of battery modules with immersion cooling, Appl. Energy 351 (2023), https://doi.org/10.1016/j.apenergy.2023.121826.
[21] J. Liu, H. Chen, M. Yang, S. Huang, K. Wang, Comparative study of natural ester oil and mineral oil on the applicability of the immersion cooling for a battery module, Renew. Energy 224 (2024), https://doi.org/10.1016/j.renene.2024.120187.
[22] E. Gonzalez-Agirre, J. Gastelurrutia, L. Oca, L. del Portillo-Valdes, L. Erbiti-Goienetxe, Dielectric flow- and tab-based battery thermal management system for EV high performance application, J. Energy Storage 87 (2024), https://doi.org/10.1016/j.est.2024.111401.
[23] J.W. Han, K.S. Garud, S.G. Hwang, M.Y. Lee, Experimental study on dielectric fluid immersion cooling for thermal management of lithium-ion battery, Symmetry (Basel) 14 (2022), https://doi.org/10.3390/sym14102126.
[24] M. Chen, W. Cheng, L. Zhao, Y. Chen, Circulating oil-immersed battery thermal management system for cylindrical lithium-ion battery module, Process Saf. Environ. Prot. 186 (2024) 200–212, https://doi.org/10.1016/j.psep.2024.04.015.
[25] G. Satyanarayana, D. Ruben Sudhakar, V. Muthya Goud, J. Ramesh, G.A. Pathanjali, Experimental investigation and comparative analysis of immersion cooling of lithium-ion batteries using mineral and therminol oil, Appl. Therm. Eng. 225 (2023), https://doi.org/10.1016/j.applthermaleng.2023.120187.
[26] Y. Liu, G. Aldan, X. Huang, M. Hao, Single-phase static immersion cooling for cylindrical lithium-ion battery module, Appl. Therm. Eng. 233 (2023), https://doi.org/10.1016/j.applthermaleng.2023.121184.
[27] H. Wang, T. Tao, J. Xu, H. Shi, X. Mei, P. Gou, Thermal performance of a liquid-immersed battery thermal management system for lithium-ion pouch batteries, J. Energy Storage 46 (2022), https://doi.org/10.1016/j.est.2021.103835.
[28] M. Larrañaga-Ezeiza, G. Vertiz, I. Galarza, H.J. Grande, P.F. Arroiabe, J. Berasategi, M. Martinez-Agirre, Partial direct liquid cooling approach for battery modules based on pouch type cells: a novel solution for electromobility applications, J. Energy Storage 121 (2025), https://doi.org/10.1016/j.est.2025.116566.
[29] J.W. Han, K.S. Garud, E.H. Kang, M.Y. Lee, Numerical study on heat transfer characteristics of dielectric fluid immersion cooling with fin structures for lithium-ion batteries, Symmetry (Basel) 15 (2023), https://doi.org/10.3390/sym15010092.
[30] J. Liu, Q. Ma, X. Li, Numerical study on heat dissipation performance of a lithium-ion battery module based on immersion cooling, J. Energy Storage 66 (2023), https://doi.org/10.1016/j.est.2023.107511.
[31] Y. Zha, S. He, X. Meng, H. Zuo, X. Zhao, Heat dissipation performance research between drop contact and immersion contact of lithium-ion battery cooling, Energy 279 (2023), https://doi.org/10.1016/j.energy.2023.128126.
[32] Z. Zou, J. Xie, Y. Luo, G. Zhang, X. Yang, Numerical study on a novel thermal management system coupling immersion cooling with cooling tubes for power battery modules, J. Energy Storage 83 (2024), https://doi.org/10.1016/j.est.2024.110634.
[33] H. Zhu, Y. Ma, J. E, S. Wei, Channel structure design and optimization for immersion cooling system of lithium-ion batteries, J. Energy Storage 77 (2024), https://doi.org/10.1016/j.est.2023.109930.

[34] X. Wu, Y. Lu, H. Ouyang, X. Ren, J. Yang, H. Guo, X. Han, C. Zhang, Y. Wu, Theoretical and experimental investigations on liquid immersion cooling battery packs for electric vehicles based on analysis of battery heat generation characteristics, Energy Convers. Manag. 310 (2024), https://doi.org/10.1016/j.enconman.2024.118478.
[35] S. Wu, L. Lao, L. Wu, L. Liu, C. Lin, Q. Zhang, Effect analysis on integration efficiency and safety performance of a battery thermal management system based on direct contact liquid cooling, Appl. Therm. Eng. 201 (2022) 117788, https://doi.org/10.1016/j.applthermaleng.2021.117788.
[36] X. Tan, P. Lyu, Y. Fan, J. Rao, K. Ouyang, Numerical investigation of the direct liquid cooling of a fast-charging lithium-ion battery pack in hydrofluoroether, Appl. Therm. Eng. 196 (2021), https://doi.org/10.1016/j.applthermaleng.2021.117279.
[37] P. Dubey, G. Pulugundla, A.K. Srouji, Direct comparison of immersion and cold-plate based cooling for automotive li-ion battery modules, Energies 14 (2021), https://doi.org/10.3390/en14051259.
[38] M. Larrañaga-ezeiza, G.V. Navarro, I.G. Garmendia, P. Fernandez Arroiabe, M. Martinez-Agirre, J. Berasategi Arostegui, Parametric optimisation of a direct liquid cooling – based prototype for electric vehicles focused on pouch-type battery cells, World Electr. Vehic. J. 13 (2022), https://doi.org/10.3390/wevj13080149.
[39] C.C. Okaeme, C. Yang, A. Saxon, J.A. Lustbader, D. Villeneuve, C. Mac, T. Reed, Thermal design analysis for SuperTruck II lithium-titanate battery pack, J. Energy Storage 56 (2022), https://doi.org/10.1016/j.est.2022.105753.
[40] M. Hussain, M.K. Khan, M. Pathak, Thermal management of high-energy lithium titanate oxide batteries using an effective channeled dielectric fluid immersion cooling system, Energy Convers. Manag. 313 (2024), https://doi.org/10.1016/j.enconman.2024.118644.
[41] Y. Li, Z. Zhou, L. Su, M. Bai, L. Gao, Y. Li, X. Liu, Y. Li, Y. Song, Numerical simulations for indirect and direct cooling of 54 V LiFePO4 battery pack, Energies 15 (2022), https://doi.org/10.3390/en15134581.
[42] H. Choi, H. Lee, J. Kim, H. Lee, Hybrid single-phase immersion cooling structure for battery thermal management under fast-charging conditions, Energy Convers. Manag. 287 (2023), https://doi.org/10.1016/j.enconman.2023.117053.
[43] B. Wu, Z. Li, J. Zhang, Thermal design for the pouch-type large-format lithium-ion batteries, J. Electrochem. Soc. 162 (2015) A181–A191, https://doi.org/10.1149/2.0831501jes.
[44] M. Ghalkhani, F. Bahiraei, G.A. Nazri, M. Saif, Electrochemical–thermal model of pouch-type lithium-ion batteries, Electrochim. Acta 247 (2017) 569–587, https://doi.org/10.1016/j.electacta.2017.06.164.
[45] A.V. Shelke, J.E.H. Buston, J. Gill, D. Howard, K.C. Abbott, S.L. Goddard, E. Read, G.E. Howard, A. Abaza, B. Cooper, J.X. Wen, Characterizing and predicting 21700 NMC lithium-ion battery thermal runaway induced by nail penetration, Appl. Therm. Eng. 209 (2022), https://doi.org/10.1016/j.applthermaleng.2022.118278.
[46] G.-H. Kim, K. Smith, K.-J. Lee, S. Santhanagopalan, A. Pesaran, Multi-domain modeling of lithium-ion batteries encompassing multi-physics in varied length scales, J. Electrochem. Soc. 158 (2011) A955, https://doi.org/10.1149/1.3597614.
[47] International Organization for Standardization, ISO 22007-2: Plastics — Determination of Thermal Conductivity and Thermal Diffusivity — Part 2: Transient Plane Heat Source (Hot Disc) Method, ISO, 2008.
[48] M. Chen, G.A. Rincon-Mora, Accurate electrical battery model capable of predicting runtime and I-V performance, IEEE Trans. Energy Convers. 21 (2006) 504–511, https://doi.org/10.1109/TEC.2006.874229.
[49] M.J. Brand, P.A. Schmidt, M.F. Zaeh, A. Jossen, Welding techniques for battery cells and resulting electrical contact resistances, J. Energy Storage 1 (2015) 7–14, https://doi.org/10.1016/j.est.2015.04.001.
[50] S. Choi, S. Lim, A. Shan, J. Lee, T.G. Yun, B. Hwang, Tab-to-Busbar interconnections in EV battery packs: an introductory review of typical welding methods, Micromachines 17 (2025) 2, https://doi.org/10.3390/mi17010002.
[51] F. He, A.A. Ams, Y. Roosien, W. Tao, B. Geist, K. Singh, Reduced-order thermal modeling of liquid-cooled lithium-ion battery pack for EVs and HEVs, in: 2017 IEEE Transportation Electrification Conference and Expo (ITEC), 2017, pp. 507–511, https://doi.org/10.1109/ITEC.2017.7993322.
[52] S.W. Churchill, H.H.S. Chu, Correlating equations for laminar and turbulent free convection from a vertical plate, Int. J. Heat Mass Tran. 18 (1975) 1323–1329, https://doi.org/10.1016/0017-9310(75)90243-4.
[53] B.M. Berkovsky, V. Polevikov, Numerical study of problems on high-intensive free convection. https://api.semanticscholar.org/CorpusID:125947621, 1977.
[54] A. Das, A. Barai, I. Masters, D. Williams, Comparison of tab-to-busbar ultrasonic joints for electric vehicle li-ion battery applications, World Electr. Vehic. J. 10 (2019), https://doi.org/10.3390/wevj10030055.
[55] Z. Geng, J. Groot, T. Thiringer, A Time- and cost-effective method for entropic coefficient determination of a large commercial battery cell, IEEE Trans. Transp. Electrif. 6 (2020) 257–266, https://doi.org/10.1109/TTE.2020.2971454.
[56] Y. Nayfeh, J.C. Vittitoe, X. Li, Quantifying the aging of lithium-ion pouch cells using pressure sensors, Batteries 10 (2024), https://doi.org/10.3390/batteries10090333.
[57] E. Michelini, P. Höschele, S.F. Heindl, S. Erker, C. Ellersdorfer, Experimental investigation on reversible swelling mechanisms of lithium-ion batteries under a varying preload force, Batteries 9 (2023), https://doi.org/10.3390/batteries9040218.